Physics-Aware Generative Adversarial Networks for Radar-Based Human Activity Recognition

M.M. Rahman, Student Member, IEEE, S.Z. Gurbuz, Senior Member, IEEE, M.G. Amin, Fellow, IEEE

Abstract—Generative adversarial networks (GANs) have recently been proposed for the synthesis of RF micro-Doppler signatures to address the issue of low sample support and enable the training of deeper neural networks (DNNs) for enhanced RF signal classification. But GANs suffer from systemic kinematic inconsistencies that decrease performance when GAN-synthesized data is used for training DNNs in human activity recognition. As a solution to this problem, this paper proposes the design of a multi-branch GAN (MBGAN), which integrates domain knowledge into its architecture, and physics-aware metrics based on correlation and curve-matching in the loss function. The quality of the synthetic samples generated is evaluated via image quality metrics, the ability to synthesize data that reflects human physical properties and generalize to broader subject profiles, and the achieved classification accuracy. Our experimental results show the proposed approach generates synthetic data for training that more accurately matches target kinematics, resulting in an increase of 9% in classification accuracy when classifying 14 different ambulatory human activities.

Index Terms—radar, micro-Doppler, generative adversarial networks, physics-aware machine learning, gait analysis

I. INTRODUCTION

Short-range radars have been widely used in a variety of applications in recent years, including border control and security, monitoring daily activities [1], sensing for smart environments [2], and human-computer interfaces [3] via gesture [4] and sign language recognition [5]. Radars are low-cost, non-contact sensors that can work remotely in an indoor environment without acquiring personal imagery of the environment or user. As a result, they are non-intrusive to the user while simultaneously enabling constant monitoring of the surrounding environment.

The classification of human activities based on their micro-Doppler [6], [7] signatures has been a key feature in all of these investigations. Because of the increased availability of memory capacity and ever-increasing processing speeds of GPUs, the use of deep learning-assisted solutions in radar signal processing has exploded in recent years. These algorithms' results are usually dependent on a substantial amount of training data of high signal-to-noise ratio (SNR). However, in practice the amount of data acquired is typically greatly limited and unbalanced due to the time and cost associated

This work was supported in part by the National Science Foundation under Award #1932547. Human studies research was conducted under University of Alabama Institutional Review Board (IRB) Protocol #18-06-1271.

M.M. Rahman and S.Z. Gurbuz are with the University of Alabama, Department of Electrical and Computer Engineering, Tuscaloosa, AL 35487 (email: mrahman17@crimson.ua.edu, szgurbuz@ua.edu).

M.G. Amin is with Villanova University, Department of Electrical and Computer Engineering, Villanova, PA 19085 (e-mail: moeness.amin@villanova.edu).

with gathering human subjects' data with radar. Moreover, the participants used to acquire training data are typically not adequately representative of the great variation in human gait resulting from differences in age, agility, height, and speed.

Consequently, there has been much work on the synthesis of micro-Doppler signatures for training deep models [8]. These works may be grouped according to two principle approaches: (1) synthesis by taking the time-frequency transform of the expected radar return computed from a skeletal model comprised of point targets animated using motion capture (MOCAP) data, and (2) direct synthesis of the micro-Doppler signature using generative adversarial network (GANs) trained from a small number of measured signatures. Model-based synthesis from MOCAP [9], [10], [11], [12], [13], [14], [15] has the advantage of allowing estimation of the resulting target micro-Doppler for any desired antenna-target geometry. Although the MOCAP data itself is still subject-specific data, a recently proposed diversification technique [16] that applies data augmentation to the underlying skeleton has allows for relatively few MOCAP measurements to be used to generate thousands of statistically independent animations, which properly span the range of expected human profiles. However, one major drawback is that model-based data synthesis does not account for changes in signal-to-noise ratio, sensor-related artifacts, non-stationary clutter, interference or signal dispersion induced by frequency-dependent barriers such as walls. In contrast, GANs have been shown effective in modeling sensor imperfections, noise and clutter in radar human activity data synthesis [17]. A wide range of GANs have been utilized in synthesizing radar micro-Doppler signatures for human motion recognition [18], [19], [20], [21].

However, previous research [20], [22] has revealed that GAN-generated RF micro-Doppler signatures exhibit systemic flaws in generation of target kinematics, which correspond to physically impossible features in the synthetic data. Examples of some of these kinematic flaws include disjoint components, malformed shapes, inconsistencies in peak values, subdued regions, and additional non-zero micro-Doppler components that make the signature resemble a different activity class altogether. A hard, impulsive fall may instead resemble a slower progressive fall. A walking signature may include a period over which the person is actually stopped and not moving at all. These kinematic aberrations can significantly degrade classification accuracy when the synthetic data is used for training. In prior work [20], we proposed a Principle Component Analysis (PCA)-based sifter that would identify outliers and remove flawed samples - removing 9,000 outliers from the 40,000 synthetic samples generated actually boosted the classification performance by %10.

This work proposes a physics-aware machine learning (PhML) [23] approach that integrates domain knowledge of human motion into the design of GAN architecture and loss functions to improve the accuracy with which human micro-Dopper signatures are synthesized using GANs. Because the envelope constrains the maximum velocity incurred during motion and differences between human gaits is captured by the envelope, it is essential that the process for generating synthetic samples consistently and realistically replicates the envelopes characteristics of ambulatory classes. Thus, we aim to preclude gross kinematic errors in synthetic samples by supplying the signature envelopes as inputs to additional branches in the discriminator and utilizing an additional physics-based loss term in the GAN loss function. While Section II provides an overview and description of PhML, Section III details physics-aware GAN design for micro-Doppler signature synthesis, proposing both architectural modifications and the utilization of physics-based metrics in the loss function. Section IV presents results for the proposed approach on a 14-class ambulatory activity recognition problem. The impact of the proposed physics-aware GAN design on accurately reflecting gait asymmetry and generalizing to physical profiles outside that of the specific test subjects used during training is evaluated. The results show that the proposed approach increases the efficacy of GAN-synthesized signatures for training deep models for human activity recognition.

II. PHYSICS-AWARE MACHINE LEARNING

Physics-aware machine learning (PhML) is an emerging field within ML that strives to integrate physics-based models with data-driven deep learning to reap the benefits of both approaches. Physics-based models represent the high level of domain knowledge gained from a study of the electromagnetic backscatter from surfaces and objects over the years. It can also capture phenomenological factors pertinent to the sensing scenario as well as known sensor properties. However, physics-based models are less adept at capturing the nuances of environment-specific, sensor-specific, or subject-specific properties. Here, deep learning can provide tremendous insight through data-driven learning.

Unfortunately, in sensing problems, it is not common to have a large volume of data. The limitations in training sample support ultimately also limit the accuracy and efficacy of deep learning in RF sensing. Moreover, no model is perfect - while more complex models could surely be developed to improve accuracy, the dynamic nature of the sensing environment ensures that there will always be some part of the signal that is unknown. This is where leveraging data-driven deep learning can provide a powerful tool when used in tandem with physics-based models. The resulting hybrid approach, PhML, combines the strengths of deep learning and physics-based modeling to optimize trade-offs (Figure 1) between prior versus new knowledge, models vs. data, uncertainty, complexity, and computation time, for greater accuracy and robustness.

Much of current literature involving physics-aware machine learning has focused on the solution of ordinary differential

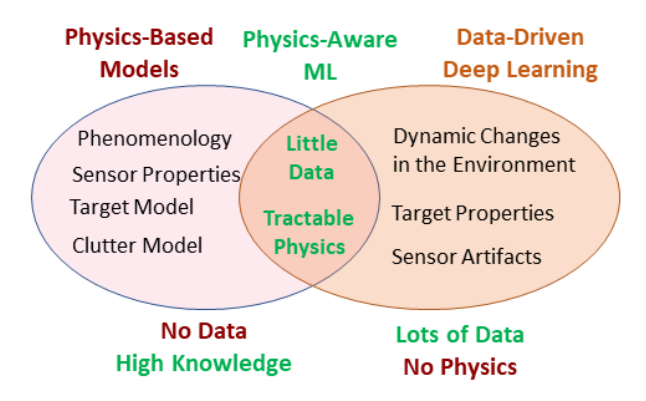


Fig. 1. The physics-aware machine learning (PhML) trade-off.

equations (ODEs) [24], [25], data-driven discovery of physical laws [26], [27], uncertainty quantification [28] and data generation. One goal is to synthesize data used for validation on simulated data in the cases where acquiring real measurements is not feasible. Another goal is for physics-guided initialization to pre-train deep models. The question of whether GANgenerated samples conform to physical constraints has recently been raised in the context of turbulent flow simulation, where both deterministic constraints (conservation laws) [29] and statistical constraints (energy spectrum of turbulent flows) [30] have been proposed for incorporation into the loss function. These constraints were shown to yield improvements in performance relative to that attained by standard GANs. This improvement was attributed to the synthetic samples accurately emulating certain physical properties of the system, while also significantly reducing (by up to %80) the training time.

This work contributes to the broad area of physics-aware GAN design via the development of architectural modifications and metrics for kinematic fidelity for loss regularization specifically to improve the accuracy in representing human micro-Doppler signatures. It builds upon prior works [31], [32], which explored the potential of adding an auxiliary branch using small-scale datasets. In [31], a multi-branch GAN taking only the upper envelope of the micro-Doppler signature was considered. Visual observation was used to examine the effect of adding an additional branch on the synthetic signatures generated, as well as the differences in feature distribution revealed using t-distributed stochastic neighbor embedding (t-SNE). A dataset comprised of 271 real samples from five different walking styles (normal walking, limping with one or both legs, walking with a cane in sync with the leg, and out of sync with the leg) was collected and utilized. It was observed that adding the additional branch caused a greater degree of overlap in the feature distributions of the real and synthetic samples. In [32], a 300-sample dataset comprised of five different walking styles (walking towards the radar, walking on toes, short steps, scissors gait, and walking with a cane) was utilized to evaluate metrics for assessing the kinematic fidelity of GAN-synthesized samples. It was shown that the inclusion of the dynamic time warping distance, discrete Frechet distance or Pearson correlation as physicsbased metrics in the loss function further increased the degree of overlap in the feature distributions of real and synthetic samples and resulted in an increase in classification accuracy.

The contributions of the current manuscript in relation to these preliminary results are

- 1) The development and comparison of architectural variants of physics-aware GANs (PhGAN): Not just the addition of a single auxiliary branch taking as input the upper envelope, but also configurations involving a single branch with the lower envelope as input, and two branches with both upper and lower envelope as input are considered. The efficacy of envelope-based metrics for capturing physics-based loss is also evaluated.
- 2) The evaluation of proposed PhGAN designs on a much larger dataset involving 14 different ambulatory classes: As such, it represents a much greater challenge of kinematic fidelity in synthetic data, which is manifested in the minute differences in the micro-Doppler signature for each type of gait and in the much higher dimensionality of the classification problem.
- 3) The detailed quantitative analysis of the characteristics of the synthetic samples: This includes an analysis of the impact of the amount and quality of the generated synthetic data. Our objective is to generate not just more data but better data. We evaluate the consistency with real signatures based on mean square error (MSE), and structural similarity index measure (SSIM), as well as gait asymmetry. We also examine the physical properties of the synthetic data samples and whether they adequately span different body sizes, as reflected in stride duration.

III. RF DATA AND PRE-PROCESSING

The data for this study were collected with a TI AWR1642 single-chip 76-GHz to 81-GHz automotive radar in an indoor laboratory environment. The radar was placed on a table 1.5 meters up from the ground facing a walkway that was 6 meters long and 3 meters wide. Data was acquired for 14 different ambulatory activities, which were articulated while moving towards the radar. These activities included various gaits (walking, short steps, walking with cane or crutches, skipping, scissors gait, walking on toes, marching, and limping) and daily activities (vacuuming the floor, dragging furniture, walking while carrying a load in one or both hands, or putting books on a bookshelf). Limping was facilitated by wrapping a leg brace around one of the legs to immobilize the knee, while a box of books was utilized as the load carried with both hands and a laptop bag was carried with just one hand. A chair was weighed down with a box of books and dragged backwards, while vacuuming involved a forward and backward movement of the vacuum. Each activity was articulated for a duration of 15 seconds and was repeated 10 times by each participant, resulting in a total of 100 samples for each activities. A total of 10 participants with varying ages, gender, height and weight participated in this study, as summarized in Table I.

The raw complex RF data were first reshaped in a 2D matrix based on the fast time and slow time samples. A Fast Fourier

TABLE I PROFILE OF PARTICIPANTS.

Subjects	Age	Height (m)	Weight (Kg)	BMI(kg/m²)
01	24	1.905	96.16	26.50
02	28	1.80	91.63	28.28
03	24	1.72	63.50	21.46
04	26	1.75	75.75	24.73
05	25	1.72	62.5	21.13
06	23	1.72	62.5	21.13
07	26	1.62	64	24.39
08	29	1.67	70	26.67
09	20	1.57	51	20.69
10	22	1.60	52	20.31

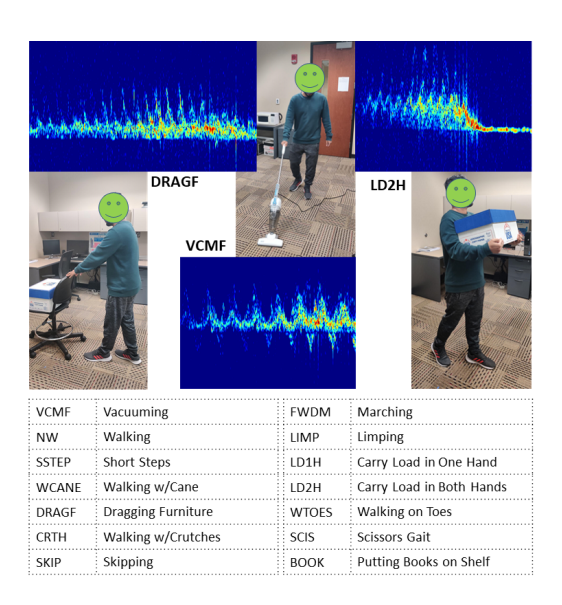


Fig. 2. Examples of acquired micro-Doppler data.

Transform (FFT) was applied in the fast-time dimension to generate the range profile. Afterwards, a fourth order butterworth high pass filter was applied to remove static clutter. Finally, the micro-Doppler signature was computed by finding the spectrogram, $S(t,\omega)$, which is the square modulus of the short-time Fourier transform, of the signal x(t), which spans the appropriate range bins. For a window function w(t), the spectrogram is found as

$$S(t,\omega) = \left| \int_{-\infty}^{\infty} w(t-u)x(u)du \right|^{2}.$$
 (1)

Several examples of the resulting signatures are shown in Figure 2.

IV. PHYSICS-AWARE GAN DESIGN FOR MICRO-DOPPLER

The baseline GAN architecture used in this work is the Wasserstein GAN with gradient-penalty (WGAN-GP) [33] because it provides stable training by minimizing an approximation of the Earth-Mover's distance (EMD) [34] rather than the Jenson-Shannon (JS) divergence [35] used in the original GAN formulation [36]. EMD is a method for evaluating the

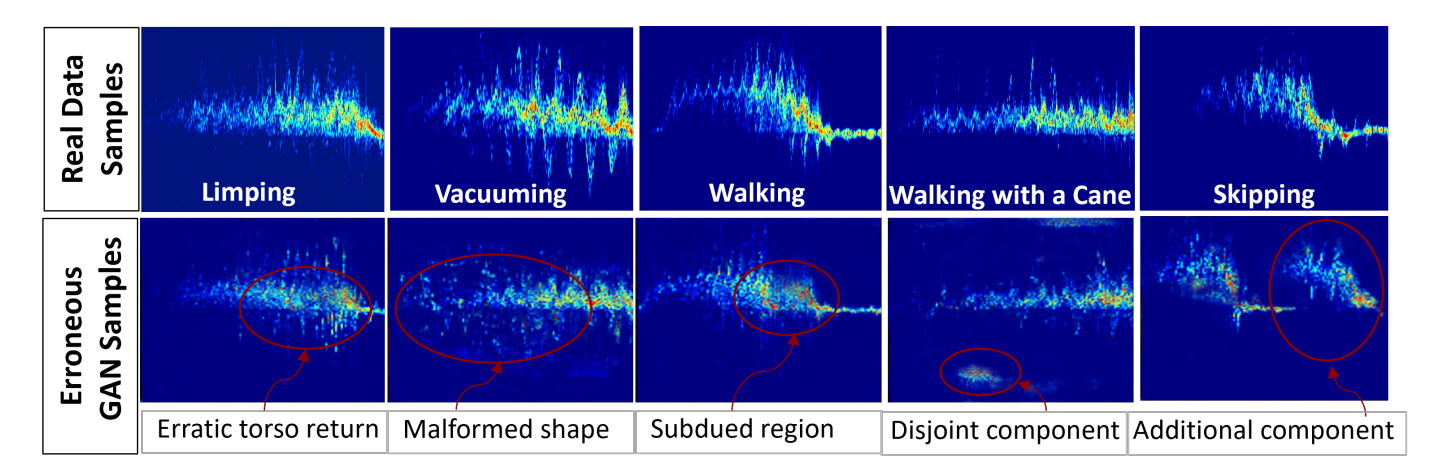


Fig. 3. WGAN-GP generated spectrograms with kinematic errors.

dissimilarity between two multi-dimensional distributions in some feature space where individual features are compared based on a given distance measure, which is known as the ground distance. If one distribution is thought of as a mass of earth in space, and the other as a collection of holes in that same space, the EMD represents the amount of work corresponding to transporting a unit of earth by a unit ground distance. Unlike JS and Kullback-Leibler (KL) divergence, EM distance offers a meaningful and smooth representation of the distance between two distributions when they are placed in lower dimensional manifolds without overlaps. As a result, even when the generator is not producing quality images, the gradients are smoother and consequently the network learns better.

The training stability of GANs can be improved by penalizing the norm of the gradient of the critic with respect to its input [37]. The Wasserstein GAN with Gradient Penalty (WGAN-GP) has been utilized widely for radar data augmentation in various applications, such as ground penetrating radar imaging [38], human activity recognition [39], [40], [41], ground target recognition [42], denoising of micro-Doppler signatures [43], and synthetic aperture radar (SAR) imaging [44]. In principle, the concepts developed in this paper could also be applied to other GAN variants.

A. Kinematic Inconsistencies in GAN-Synthesized Samples

Although the distance measures utilized in the WGAN-GP architecture capture the statistical distance between the distributions of features, these features may not directly relate to the physical properties of human movements. The micro-Doppler signature provided at the input to a GAN is just an image-based representation of frequency versus time. The features automatically learned by a GAN trained based on statistical distance thus capture spatial relationships between pixels in the input images. They do not embody physical constraints imposed by the structure of the human body, joint rotations, or the expected electromagnetic backscatter. Consequently, it is perhaps not surprising that WGAN-GP generated signatures results in synthesis of signatures whose features are statistically similar but physically erroneous.

As an example, consider the WGAN-GP synthesized signatures shown in Figure 3 for five different classes of human activity. Key features that set apart many human gaits are the torso and leg dynamics. Yet in many of these signatures, the torso and leg trajectories are obscured, erratic, malformed, and do not reflect a received power level that is consistent with distance. Other physically impossible flaws in the data include disjoint components, which would not be possible because the human body is a connected system, or rearrangements of the data so that the signature corresponds to a different activity. For example, the skipping signature shown in Figure 3 includes an interval of zero Doppler frequency, which corresponds to a person skipping, stopping and then potentially doing a different motion - not to continuous skipping.

While kinematic sifting can be devised to remove outliers and boost classification performance [20], the objective of the proposed physics-aware GAN design is to preclude the generation of such physically inconsistent samples in the first place.

B. Architectural Modification

Micro-Doppler signatures represent the variation of radial speed versus time of each point on the body from which the RF signal is backscattered. Thus, the upper envelope provides an upper bound on maximum speed towards the radar, while the lower envelope indicates the maximum speed away from the radar. Accuracy in synthesizing signature envelopes is significant not only due to the aforementioned physical reason, but also because the differences in human gait is primarily captured by the motion of the legs, which provides the dominant trajectory reflected in the signature envelope. Important micro-Doppler features, such as average velocity, maximum foot swing velocity, period, the phase between leg and torso, foot swing time, the range profile Doppler frequency, total bandwidth of the Doppler signal, offset of the total Doppler, normalized standard deviation of the Doppler signal strength, and period of the limb motion are all derived from the micro-Doppler signature's envelope [45], [46]. Thus, ensuring consistency in the envelop of synthesized signatures

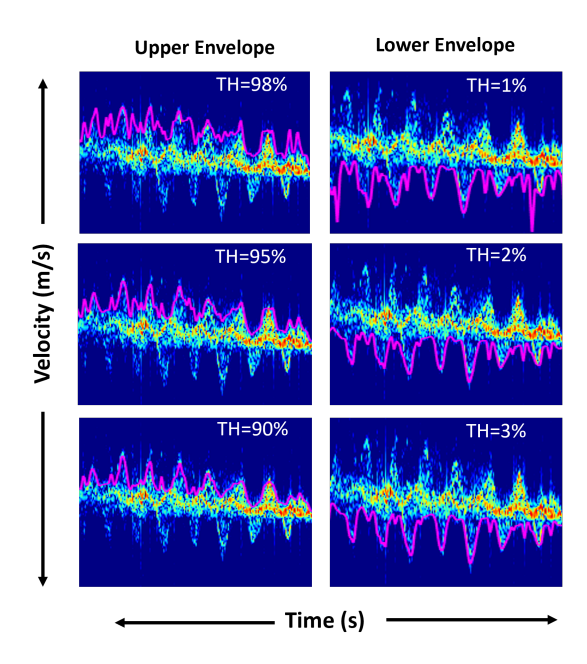


Fig. 4. Upper and lower envelope extraction at different threshold conditions.

with that of measured data is essential for enabling accurate recognition of human gait.

The envelope for a real or synthesized micro-Doppler signature can be extracted by using an energy threshold method [47] in which for each slow time index, all energy of each fast time sample is accumulated, and the envelope is identified when the summation exceeds the 90% or 3% of the total energy for the upper and lower envelope, respectively. The effect of the threshold (TH) on the extracted envelopes is illustrated in Figure 4. Notice that the use of more stringent thresholds (e.g. upper 98%/ lower 1%) results in closer tracing of minute fluctuations in the signature. This may result in over-fitting the envelope and accentuation of movements not fundamental to the gait being synthesized. Selection of a threshold too lax, however, could result in over smoothing of key envelope features. The threshold utilized in this work was selected so as pick up the gross movements of the legs, while avoiding rapid fluctuations.

To inform the GAN of envelope-based features, we propose adding additional branches to the discriminator that take as input the envelope, thereby influencing decisions on how fake or real the generated samples are. In the single-envelope Multi-Branch GAN (MBGAN), only one additional auxiliary branch taking the upper envelope as input is added. In the dual-envelope MBGAN, both upper and lower envelopes are provided as inputs to two additional auxiliary branches in the discriminator. Both variants are depicted in Fig. 5.

The generator first synthesizes samples from a 100-dimensional latent space noise vector. These generated samples are passed into the discriminator's main branch. The envelope is used as input to the auxiliary branch, which extracts features, and flattens the outputs before concatenation with the features from the main branch. All features are passed into the final dense layer. Then, the discriminator takes the batch of real samples and their envelopes to compare the similarities

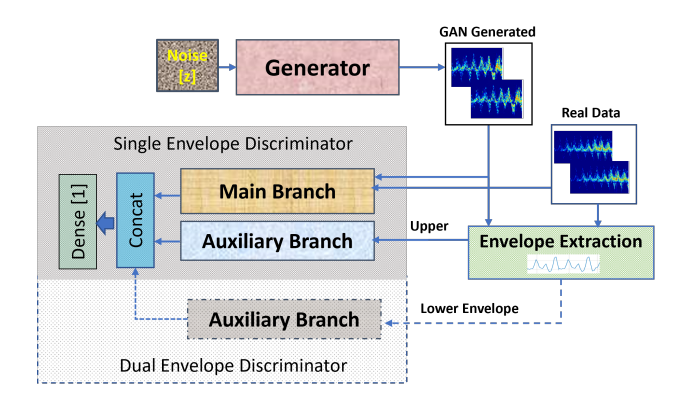


Fig. 5. Single and Dual Envelope MBGAN.

between the distribution of real and fake signatures. Based on this comparison, the discriminator scores whether the samples are fake or real on a scale of 0 to 1. The detailed structure of the generator and multi-branch discriminator is shown in Figure 6. The generator consists of 10 2D-convolutional layers, where each of the layers are followed by a batch normalization with 0.9 momentum and a Rectified Linear Unit (ReLU) activation function with the exception of the last convolutional layer, which is only followed by a tanh activation function. The number of filters, kernel and stride size for each layer are labeled over each convolutional unit in Figure 6 using the notation "n (#filters) k (kernel size) and s (stride size)". The main branch of the discriminator is an 7-layer CNN, where each layer is followed by a Leaky-ReLU activation function. The auxiliary branch is comprised of three 1D-convolutional layers. The outputs of the dense layers are concatenated with the flattened output of the main discriminator. The features extracted by the main branch of the discriminator are flattened and vector-concatenated with the features extracted from the 1D envelope in the auxiliary branch.

C. Modification of Loss Function

Another way in which GANs can be informed about physics-based constraints is through modification of the loss function over which the weights are optimized. Current state-of-the-art GAN formulations utilize statistical measures of distance when computing loss. For example, the loss function for a standard WGAN-GP architecture utilizes a loss function of the following form:

$$L_D = \{D(x) - D(G(z))\} + GP \tag{2}$$

where L_D is the critic loss and GP is the gradient penalty given as,

$$GP = \lambda \Big(||\nabla_{\hat{x}} D(\hat{x})|| \Big)^2, \tag{3}$$

In the above expression, D(x) is the discriminator's estimate of the probability that real data instance x is real; G(z) is the generator's output when given noise z; D(G(z)) is the discriminator's estimate of the probability that a fake instance is real.

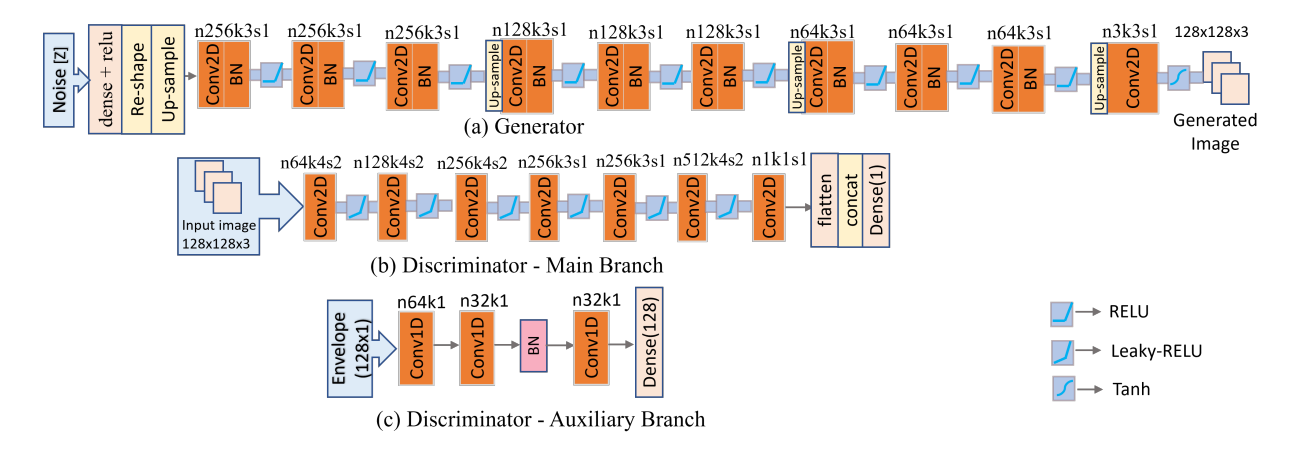


Fig. 6. Architecture of the Generator and the Discriminator's Branches. (BN: Batch Normalization, n: number of filters, k: kernel size, s: stride).

However, statistical similarity between real and synthetic samples does not necessarily guarantee physics-based similarity or conformity with physical properties. Because the statistical similarity metrics take as input images of the micro-Doppler signature, the resulting distance metrics are more reflective of spatial similarity. Thus, a key element of physics-aware design is to reformulate the loss function to include a physics-based loss term that can inform the network of errors that are not captured by the critic loss. In this case, the new proposed loss function is

$$L_D = \{D(x) - D(G(z))\} + GP + \lambda_P L_{physics}, \quad (4)$$

where $L_{physics}$ is the physics-based loss term regulated with the hyperparameter λ_P . Most generally, the physics-based loss is defined as any computable metric that is indicative of how well the synthetic samples resemble the real samples. Because the approach proposed in this work focuses on accurate representation of physical bounds on velocity, as determined by the micro-Doppler signature envelopes, the physics-based loss term is designed as a metric that captures the degree of similarity between the envelopes of synthetic and real micro-Doppler signatures.

D. Physics-Based Distance Metric

If the envelope is considered as a time-series or a curve, the choice of the distance metric is tied to the ability of the metric to produce a significant quantitative difference between the two envelopes based on how dissimilar/similar they are. In prior work [32], curve matching based distance metrics were shown to outperform correlation based metrics. In this work, three different distance metrics have been compared in terms of their ability to quantify the similarity of envelopes across all classes:

Dynamic Time Wrapping (DTW) distance: DTW measures the similarity between two temporal sequences that do not sync up with each other perfectly due to the variation in time or speed. To determine the similarity independent of certain non-linear fluctuations,

- the sequences are "warped" non-linearly in the time dimension.
- 2) Discrete Fréchet Distance (DFD): Discrete Fréchet distance [48] is a measure of similarity between curves that consider both the location and ordering of the points along the curves. DFD takes into account the flow of the two curves because the pairs of points whose distance contributes to the Fréchet distance sweep continuously along their respective curves. This makes it a better measure of similarity for curves.
- 3) Euclidean Distance: Euclidean distance is calculated as the square root of the sum of the squared differences between the two vectors. It is also known as the L2-norm.

To evaluate which metric exhibited the greatest sensitivity and separation across classes, a subset of 100 WGAN-GP synthesized samples are randomly selected for each of the 14 classes of activities recorded in this work. For each synthetic sample, the DTW, DFD, and Euclidean distances between the envelopes of the synthetic sample and each real test sample is computed and averaged. The mean value of each distance metric for each activity class is plotted as a marker for each

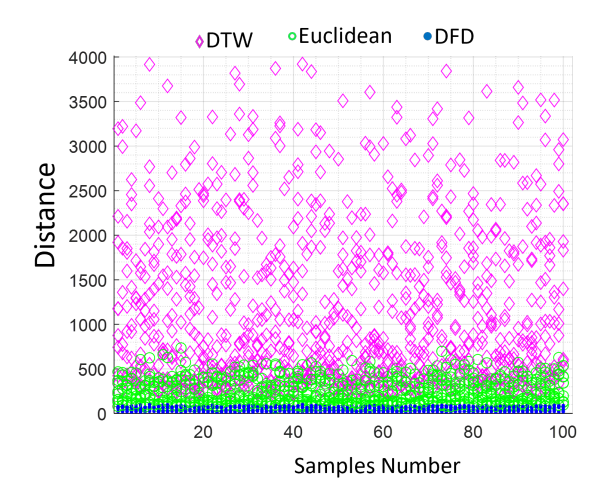


Fig. 7. Distance Metrics Comparison.

synthetic sample, as shown in Figure 7. This way of visually representing the mean distance metrics allows interpretation of sensitivity across synthetic samples, metric utilized, and each activity class. Observe that the values reported for both Euclidean distance and DFD do not exhibit much spread across classes, clumping up below a distance of 500 for each synthetic sample. In contrast, the DTW exhibits great numerical spread across values of 100 to 4000, with the 14 markers for each class given a particular sample also being visually differentiable. Consequently, the DTW is selected as the preferred metric for computing physics-based loss.

E. Depth of Networks

The influence of the depth of the generator and discriminator on the kinematic fidelity of the resulting synthetic images is evaluated through an ablation study in which the generator and discriminator depths are independently varied and the resulting DTW metrics compared. First, the depth of the discriminator in the baseline WGAN-GP model was fixed at a depth of 7, while the generator was varied between depths (D) of 4 and 10. The resulting DTW distance and network complexity, as indicated by the number of trainable parameters, is tabulated in Table II for the class "vacuuming the floor." As the generator depth increases, the matching between the real and synthetic signature envelopes, as measured via the DTW distance, improves. Thus, a generator depth of 10 layers is selected, while the depth of the discriminator is varied between 4 and 7 layers. Increasing the depth of the discriminator also resulted in a continual decrease in the DTW distance, implying a better match between synthetic and real envelopes. Thus, a depth of 7 layers was used for the main branch of the discriminator. Because the use of deeper models increases the chance of mode collapse, a generator network depth beyond 10 and discriminator network depth beyond 7 was not selected.

The impact of the depth of the auxiliary branches is also shown in Table II. Increasing the depth to three layers results in significant improvement in envelope matching, as indicated by the decrease in DTW distance. Thus, three convolutional layers were utilized in the auxiliary branches of both the single and dual MBGAN architectures.

TABLE II $\begin{array}{c} \text{Ablation study on the Generator and Discriminator} \\ \text{Architecture.} \end{array}$

	Generator		Discriminator										
			Main Branch			Main Branch+ 1 Aux. Branch				Main Branch+ 2 Aux. Branches			
D	DTW	#Params	D	DTW	#Params	D	DTW	#Params	D	DTW	#Params		
4	1702.1	14.7M	4	1883.8	0.6M	1	1184.8	3.95M	1	1380.4	3.963M		
5	1521.7	15.38M	5	1666.0	1.25 M	2	1020.3	3.951M	2	1197.7	3.965M		
6	1307.2	15.97 M	6	1507.5	1.84 M	3	837.4	3.952M	3	910.94	3.967M		
7	1102.8	16.11 M	7	963.2	3.93 M								
8	1088.0	16.26 M											
9	1000.0	16.30 M											
10	946.7	16.34 M											

^{*} D: Depth; DTW: DTW distance; # Params: No. of Trainable Parameters

V. OTHER DESIGN CONSIDERATIONS

The efficacy of the proposed MBGAN architecture with regularized physics-aware loss was validated on a fourteen-class human activity micro-Doppler dataset. In this section, first the radar system and experimental procedure utilized for data collection is described. Next, specific considerations that relate to the efficacy of the design are evaluated in turn: namely, the efficacy of envelope extraction in noise, the effect of the auxiliary branch and physics-aware loss on GAN training convergence, model complexity and training time.

A. Envelope Extraction in Noise

An important factor in real-world environments is the clutter and noise present in the spectrogram, which could result in masking of the envelopes and hence degrade the fidelity of envelope extraction. Although ground clutter is filtered out, the power of the received RF signal attenuates proportionally to $1/R^4$, where R is the distance between the person and the radar. In this case, the background of the spectrogram will appear increasingly noisy (or, conversely, the motion signature increasingly weak). To examine the effect of noise on envelope extraction, Gaussian noise with varying power is added to the measured images to generate signatures with signal-tonoise ratio (SNR) varying between 1 dB and 13 dB. Then, an adaptive 2D Wiener filter [49] for kernel size (5,5) is used to mitigate noise prior to envelope extraction.

The efficacy of envelope extraction is quantified by computing the DTW distance between the envelopes of the noisy and noiseless spectrograms. As shown in Figure 8, application of the Wiener filter enables envelope extraction to be effectively accomplished for SNRs above 3dB. For 3 dB to 13 dB, the

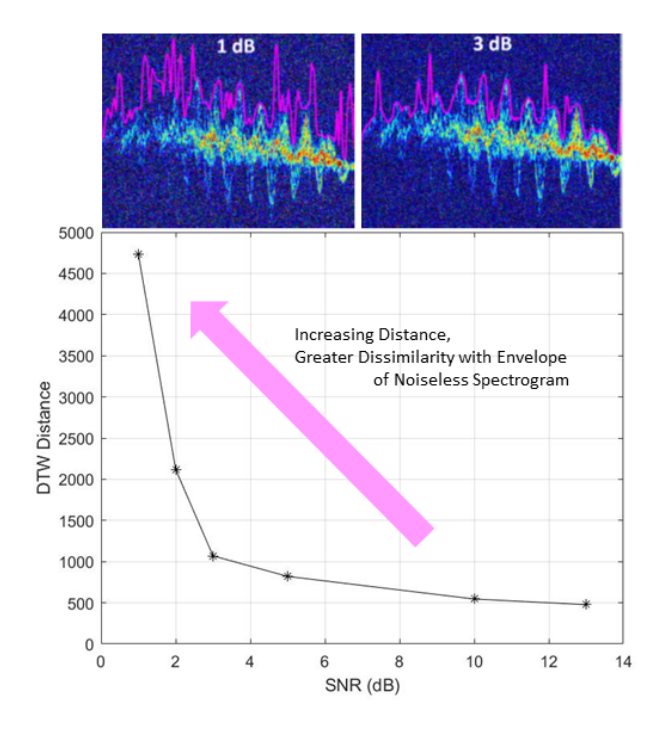


Fig. 8. Effect of noise on accuracy of extracted envelope as quantified by DTW distance between envelopes of noisy and noiseless signatures.

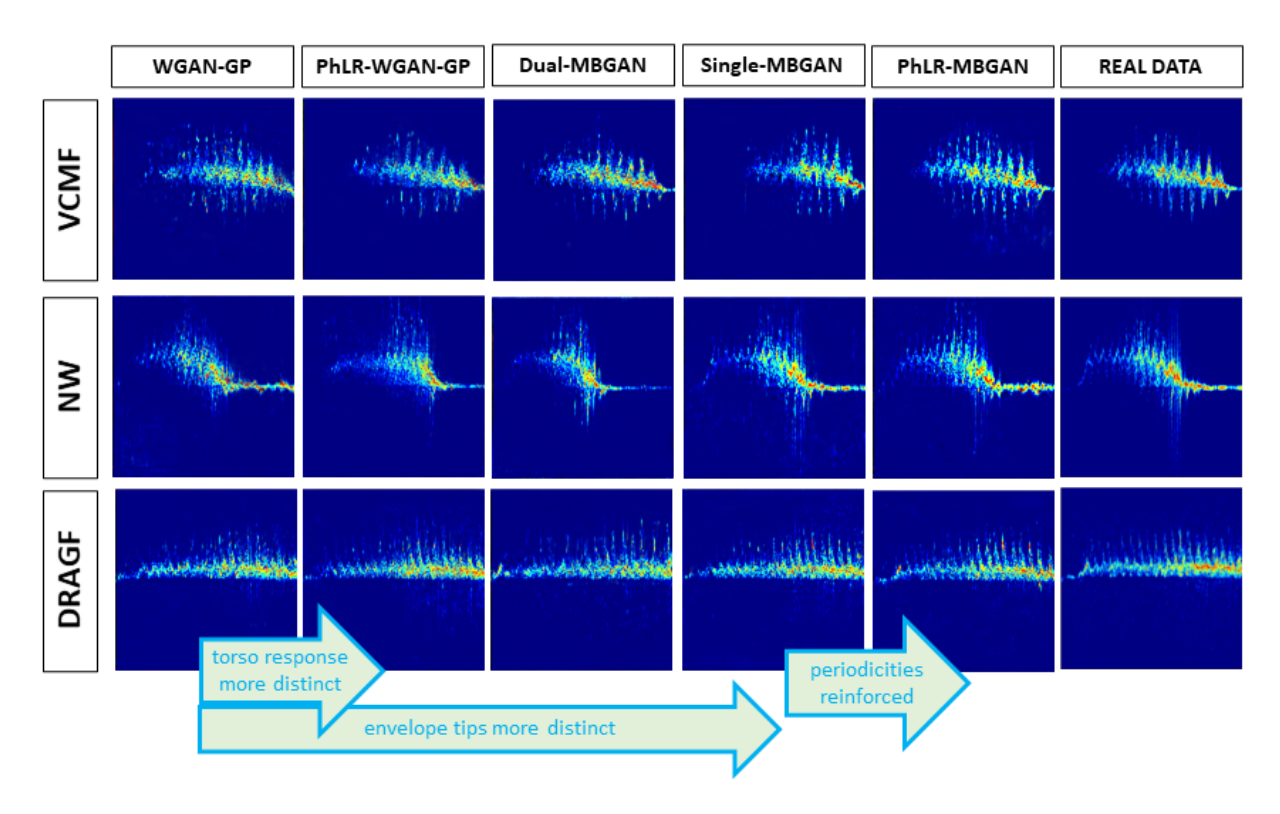


Fig. 9. Comparison of synthesized signatures generated from several GAN variants and proposed PhLR-MBGAN architecture.

DTW distance varies between 477 and 1069. But lower than 3 dB, for each single decibel reduction in SNR, the DTW distance doubles, resulting in an exponential increase in the distance from the noiseless spectrogram. Below 3 dB, the extracted spectrogram visually appears increasingly random, as opposed to conforming to the salient micro-Doppler profile. For the indoor environment considered in this work, a 10 dB drop in SNR would occur when the person was roughly twice the distance - i.e., 12 meters away. Implementation of more sophisticated envelope extraction and denoising techniques, however, would extend the range of efficacy.

B. Training of GAN Models

The generator, main and auxiliary branch discriminator were built using Keras 2.3.1 Functional API with TensorFlow 2.2.3 backend. The Codes were run on a *TITAN v3* GPUs. The envelope extraction can be done using python and pass it as an input into the discriminator, or can be directly implemented using Keras Lambda layers within the discriminator. The generator and the discriminator were trained with an Adam optimizer [50] with a learning rate of 0.0001, β_1 of 0.5 and β_2 of 0.9. For training, 80% of measured data were utilized. While training the GAN, an ablation study was conducted which comprises of the following training scenarios:

- 1) **Baseline WGAN-GP:** The WGAN-GP architecture [51] was trained as a baseline model with a gradient penalty λ of 10 and a training ratio of 5 (discriminator iteration per generator iteration).
- PhLR-WGAN-GP: In this architecture, the discriminator loss of WGAN-GP is modified by adding physics-based

- loss regularization computing using the DTW distance between the envelopes of real and GAN-synthesized samples. The regularization parameter λ_P is empirically selected as 0.1.
- 3) Single-MBGAN: In this architecture, the upper envelope is provided as input to a single auxillary branch, while the main discriminator branch takes as input the micro-Doppler signature. The auxillary branch is comprised of 1D convolutional blocks, as shown in figure 6(c), before it is concatenated with the main branch discriminator. The loss function is not modified, remaining the same as that used in WGAN-GP.
- 4) Dual-MBGAN: In this case, the discriminator is comparised of two auxiliary branches, which take as input the upper and lower envelopes of the micro-Doppler signature. Both auxiliary branches consist of 1D convolutional blocks, where the outputs are concatenated with that of the main branch of the discriminator.
- 5) **PhLR-Dual-MBGAN:** This architecture includes both the upper and lower envelopes as two auxiliary discriminator branches. Consequently two physics-based loss terms for each envelope are added in Equation 3 and regularised with the same λ_P .
- 6) PhLR-MBGAN: This architecture includes both an auxiliary discriminator branch taking as input the upper envelope, as well as the physics-based loss regularization using the DTW distance.

A comparison of the signatures generated using the aforementioned architectures is given in Figure 9. WGAN-GP signatures exhibit weak depiction of the envelopes and the torso

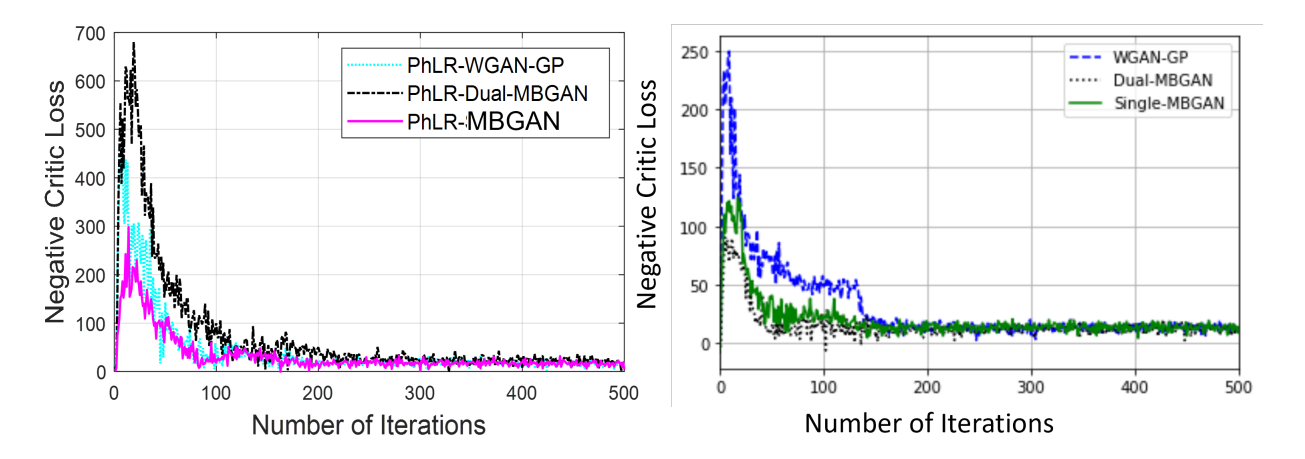


Fig. 10. Convergence of GAN training.

response, which is represented by the strongest (peak) return in the signature (usually colored reddish). When a physics-based loss term is added to the WGAN-GP architecture, the torso response becomes more evident and the depiction of leg swings is improved - but not yet well enough to be comparable to the real data. The addition of auxiliary branches further improves the envelope and strengthens the torso response. However, it is only when the upper envelope is utilized in an auxiliary branch, while the loss function is also augmented with a physics-based loss term, that the resulting synthetic samples closely resemble the read data, and is especially adept at synthesizing each peak in the micro-Doppler shift distinctly and accurately.

C. Convergence and Computational Complexity

When the model loss does not settle down during the training process, a neural network fails to converge. A failure to converge in the case of a GAN refers to the discriminator and generator failing to find an equilibrium. The most common way to identify this type of failure is that the loss for the discriminator has gone to zero [52]. The most prevalent cause of this type of loss is the generator producing junk images that the discriminator can easily detect.

To assess the impact of the architectural modifications and physics-based loss term on network training and convergence, the discriminator losses observed in each architecture are compared in Figure 10.

During the training of all the GAN scenarios, the following discriminator losses are observed as shown in Figure 10. The discriminator loss is stable and non-zero for all of them, which indicates the convergence of GAN. For PhLR-WGAN-GP and PhLR-MBGAN, the loss drops to 77 and get into stable stage at around 150 iterations. On the other hand, Single and Dual-MBGAN reached to the stable training earlier compared to the WGAN-GP and the stable training is achieved when the discriminator loss drops to around 13.71.

However, the inclusion of envelopes as auxiliary branches in discriminator increases the number of trainable parameters and hence increases the training time. For instance, to reach to 10000 iterations, WGAN-GP takes 25 minutes, whereas single envelope MBGAN & PhLR-MBGAN takes 48 minutes and dual-envelope MBGAN takes 73 minutes. All the models have been trained for 40,000 iterations to generate the final synthetic signatures.

VI. RESULTS AND ANALYSIS

In this section, the effect of the multi-branch discriminator and physics-based loss function is quantified using standard image metrics, classification accuracy and the gait abnormality replication capability.

A. Quality measures of GAN Synthesized Signatures

The quality of micro-Doppler spectrograms synthesized by the different GAN models are quantified by measuring mean square error (MSE) [53]and structural similarity index metric (SSIM) [54] between the real and GAN generated signatures.

$$MSE = \frac{1}{N_x N_y} \sum_{x,y} [R(x,y) - S(x,y)]^2$$
 (5)

$$SSIM = l(R, S)^{\alpha}.c(R, S)^{\beta}.s(R, S)^{\gamma}$$
 (6)

$$MSSIM = \frac{1}{N_x N_y} \sum_{x,y} SSIM(R,S)$$
 (7)

where, R(x,y) and S(x,y) are the real and synthetic image and N_x and N_y are the height and width of the image. l,c,r refer to luminance, contrast and structural measures, and $\alpha=\beta=\gamma=1$. A total of 200 synthetic samples are randomly chosen for each class and the mean MSE and mean SSIM (MSSIM) are measured comparing with the real test images using Equations 5 and 7. Table III shows the quality measures using MSE and SSIM for all the scenarios of GAN models described in subsection V-B. These numbers can be better visualised with the box-plot of Figure 11, which shows that the PhLR-MBGAN generated signatures with the greatest similarity and lowest MSE relative to the real test samples. In this fashion, WGAN-GP which is the baseline model, generates signatures with lower structural similarity and higher MSE.

GANs	Metric ID:	VCMF	NW	SSTEP	WCANE	DRAGF	CRTH	SKIP	FWDM	LIMP	LD1H	LD2H	WTOES	SCIS	воок
	SSIM	0.8095	0.731	0.7329	0.7764	0.7944	0.77	0.80	0.72	0.77	0.81	0.79	0.77	0.79	0.86
PhLR-MBGAN	MSE	522.95	575	581.98	441.18	473.94	467.59	480	578	523.05	454.17	495.33	514.76	515.67	368.41
PhLR-Dual	SSIM	0.7603	0.71	0.6941	0.7706	0.7686	0.7162	0.7576	0.663	0.7375	0.7651	0.7558	0.756	0.741	0.82
MBGAN	MSE	629.47	958.72	885.99	576.06	535.75	758.78	762.74	859.1	821.03	772.12	773.09	853.04	897.82	483.93
Single-MBGAN	SSIM	0.7613	0.7040	0.6833	0.7795	0.7636	0.72	0.75	0.66	0.73	0.76	0.75	0.74	0.73	0.82
Siligle-MBGAN	MSE	658.38	1031.7	873.11	614.02	577.16	753.67	784	875.8	857.33	825.53	830.19	843.50	951	503.98
Dual-MBGAN	SSIM	0.7549	0.6836	0.6724	0.7736	0.7686	0.7076	0.745	0.64	0.72	0.76	0.74	0.72	0.72	0.83
Dual-IVIDGAIN	MSE	771.78	1078.1	871.77	623.70	719.31	828	871.45	925.3	979	894.68	879.20	876	928.6	551.38
PhLR-WGAN-GP	SSIM	0.7573	0.6818	0.6678	0.7763	0.7578	0.701	0.74	0.64	0.73	0.76	0.74	0.70	0.72	0.82
	MSE	800.92	1025.9	874.01	620.31	727.08	811.13	876.19	929.7	891.04	927	898.73	905	895.33	562.13
WGAN-GP	SSIM	0.755	0.6819	0.6480	0.7731	0.7537	0.712	0.734	0.64	0.715	0.75	0.74	0.71	0.72	0.81
	MSE	748.16	1013.0	872.53	666.06	775.15	883.04	906.05	943.4	857.17	948.06	908.32	872.34	930.52	619.97

TABLE III
QUALITY MEASURES OF GAN SYNTHESIZED SIGNATURES.

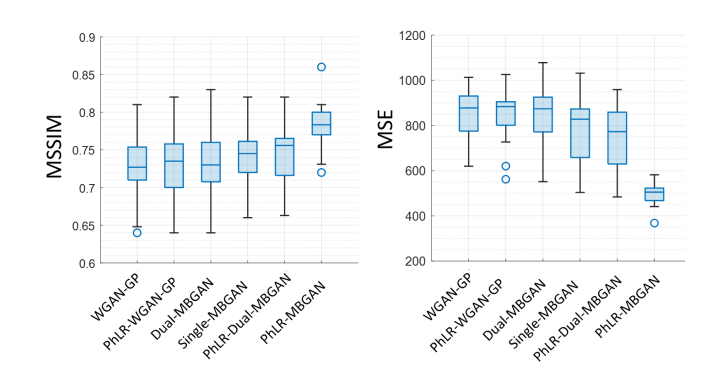


Fig. 11. Box plot to compare SSIM and MSE for all the GAN models .

B. Classification Accuracy

Another way to evaluate the efficacy of GAN-synthesized signatures is to consider the resulting classification accuracy the better the synthetic signatures, the higher the classification accuracy. A convolutional auto-encoder, which consists of 3 convolutional blocks, is utilized for classification due to its efficacy in classifying datasets with low training sample support [55]. In each block, there are two convolutional layers, followed by a concatenation and a maxpooling layer. The concatenation technique provides multilevel feature extraction. CAEs use unsupervised pre-training to initialize the network near a good local minima. After training the CAE model, the decoder was removed, the output of the encode is flattened and two fully connected layers with 128 and 64 neurons are added, each of them are followed by a dropout of 0.65 and 0.55 respectively. At the output, a softmax layer with 14 nodes is employed for classification. During training, the ADAM [50] optimizer was utilized, along with a batch size of 64, learning rate of 0.00008 and 70 epochs.

Table IV shows the classification accuracy achieved when training the CAE separately with the synthetic data generated by all 6 GAN variants and testing with the real data that has not been utilized in GAN training. Of the 100 real samples per class, 80% is reserved for training, while 20% is utilized

TABLE IV
CLASSIFICATION ACCURACY USING CAE WHILE TRAINING WITH
GAN-SYNTHESIZED DATA.

GAN	Real	Accuracy (%)											
Samples	Data	PhLR- MBGAN	PhLR-Dual MBGAN	Single- MBGAN	Dual- MBGAN	PhLR- WGAN-GP	WGAN- GP						
	0	48.57	47.86	44.29	43.93	40.88	38.21						
	224	78.57	75.71	75.00	74.43	73.57	72.86						
7000	448	81.86	77.50	76.79	76.07	75.29	74.00						
	672	84.57	81.79	81.50	81.07	78.93	77.50						
	896	86.79	84.29	83.57	82.50	82.14	81.43						
	1120	89.23	86.50	86.07	85.71	84.64	84.29						
0	1120		Accuracy while training only on the real data: 80.36 %										

*Total Real training samples: 1120; GAN Synthesized Samples: 7000; Test samples: 280

in testing. Thus, 80 samples per class are used to train a GAN, which is, in turn, generates 500 synthetic samples per class. As more real data is utilized together with the GAN-synthesized samples for training, the resulting classification accuracy increases. Whereas training on GAN-synthesized samples alone results in 48.57% accuracy, the inclusion of real samples increases the accuracy to as high as 89.23%. However, if only real data is used during training, an accuracy of just 80.36% is achieved. Thus, the proposed approach results in a 9% performance improvement over the use of real data alone.

The PhLR-MBGAN model shows superior accuracy compared to all other methods, which reflects the efficacy of the modified discriminator and loss function. The addition of one auxiliary branch increases accuracy by 3% as compared to the baseline WGAN-GP model. The effect of utilizing different discriminator architectures is captured by Table V, which provides not just the resulting classification accuracy but also a comparison of image quality metrics. For this ambulatory dataset, the dual-branch variant actually results in a slightly lower accuracy, indicating that the lower envelope does not capture any significant kinematic features. This makes sense for this dataset, as all activities were conducted towards the radar, resulting in a pre-domominantly positive micro-Doppler signature. It is also interesting to note that just

adding a physics-based loss term without any architectural modifications does not make a significant impact, as may be observed by comparing the results of the WGAN-GP with that of the PhLR-WGAN-GP.

The effect of utilizing varying amounts of GAN-synthesized data is shown in Figure 12. Although utilizing an increasing number of synthetic samples in training does increase the accuracy, it may be observed that beyond 5,250 samples, the curve begins to flatten, implying less benefit in using additional synthetic samples.

C. Impact of Aspect Angle on Optimal PhGAN Architecture

In this study, all activities were articulated toward the radar. Therefore, it is necessary to assess the performance of the proposed MBGAN in synthesizing spectrograms for activities performed at different directions and aspect angles. Towards this aim, participants were asked to walk away from the radar along the radar line-of-sight and along a skewed diagonal. A total of 100 samples for each angle were collected, 80% of which were used in GAN training. Then the GAN synthesized samples were generated using the PhLR-MBGAN with an upper envelope as an auxiliary branch, a lower envelope as an auxiliary branch, and both envelopes as two auxiliary branches. An example of PhLR-MBGAN (lower envelope) synthesized sample is shown in Figure 13. A total of 500 samples were generated for each case. The quality of the generated signatures is evaluated with SSIM and MSE metrics, which are tabulated in Figure 13. For motion articulated away from the radar, the micro-Doppler signature contains predominantly negative frequencies, and the key kinematic features are captured by the lower, not the upper envelope. Thus, the utilization of a single auxiliary branch taking as input the lower envelope offers better quality synthetic samples than using the other two variants, including that of the dualauxiliary branch PhLR-Dual-MBGAN.

When the person walks along a diagonal, however, there is a greater balance between positive and negative frequencies, thus the gap between the GAN variants is reduced. In this case, the use of the lower envelope alone only slightly surpasses that of using both envelopes in a dual branch architecture. These results show that while the selection of an auxiliary branch taking as input of the upper or lower envelopes is primarily dependent upon the dominant direction of motion (towards or away), the precise angle at which the person is moving does not have a significant impact on the preferable architecture. When there is no dominant direction or a balance in positive and negative Doppler components is expected, a dual-branch architecture may be preferred.

D. Effect of Envelope on Gait Asymmetry

In the case of normal walking, the reflection from both legs is equal and hence symmetric nature of walking is observed in spectrograms. However, in the case of any gait abnormality, the weaker leg moves slowly towards the radar, compared to the stronger foot, hence the reflection from that leg will be much less compared to the strong foot. Therefore, gait asymmetry is visible in the micro-Doppler signatures. The asymmetry index

TABLE V Ablation study on Discriminator module.

Discriminator Module	GAN Models	Training convergence Epoch No.	Accuracy(%)	Mean SSIM	Mean MSE
Main Branch Only	WGAN-GP	150	84.29	0.7245	853.12
Main Branch + PhLR	PhLR-WGAN-GP	150	84.64	0.7280	838.89
Main Branch+ 2 Auxiliary Branch	Dual-MBGAN	50	85.71	0.7311	842.73
Main Branch+ 1 Auxiliary Branch	Single-MBGAN	50	86.07	0.7394	784.24
Main Branch+ 2 Auxiliary Branch+PhLR	PhLR-Dual- MBGAN	250	86.50	0.7440	754.83
Main Branch+ 1 Auxiliary Branch+PhLR	PhLR-MBGAN	150	89.23	0.7803	499.43

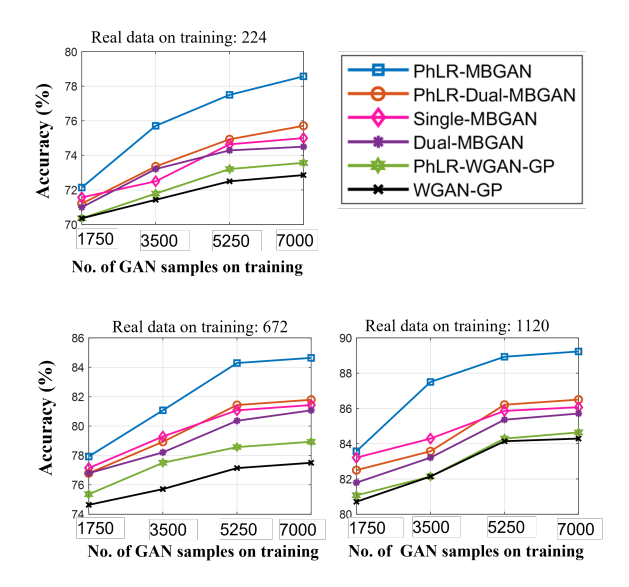


Fig. 12. Effect of utilizing varying amounts of real and GAN-synthesed data for CAE training on resulting classification accuracy.

Real Data	Away straight	Away Diagonally	GANs	Walk Stra	Away iight	Walk Away Diagonally	
	Marin			SSIM	MSE	SSIM	MSE
			PhLR-MBGAN (Lower Envelope)	0.75	531.22	0.7304	552.86
Synthesized	1		PhLR-MBGAN (Upper Envelope)	0.70	787.05	0.695	827.21
GAN Sy			PhLR-Dual-MBGAN	0.747	608.71	0.720	636.18

Fig. 13. Effect of direction and aspect angles on PhLR-MBGAN synthesized Data. (Left) PhLR-MBGAN (lower envelope) synthesized samples. (Right) Image quality assessment usign SSIM MSE.

(ASI) is measured based on the spread of Doppler frequency of stronger and weaker feet using the following formula [56]:

$$ASI = \frac{|DS_{Weak} - DS_{Strong}|}{DS_{Strong}} 100\%$$
 (8)

where DS_{Weak} and DS_{Strong} stand for the Doppler shift of weaker and stronger foot respectively. For each spectrogram, an average ASI is calculated from all the pairs of strong and weak foot's Doppler shift. For the class 'walking with crutches,' Figure 14 shows that the PhLR-MBGAN synthesized signatures better span the variations in ASI represented by the real data samples than the baseline WGAN-GP synthesized signatures.

Since this gait asymmetry is captured in an upper envelope, the PhLR-MBGAN should produce signatures with the same degree of asymmetry as real spectrograms. In the contrary, WGAN-GP generated signatures lack adequately replicating this gait asymmetry. The box plot in Figure 8, shows that the first and 3rd quartile of ASI index for all the samples from PhLR-MBGAN fall within the first and third quartile of real samples. The median of PhLR-MBGAN (0.3) is also close to the real sample's median (0.35). In contrast, the median ASI of WGAN generated samples is 0.2, which is off by about 0.15 compared to the real samples. These statistics indicate how effectively the envelope feature captures the micro-Doppler properties. In this case, the gait asymmetry is replicated very effectively with the proposed physics-aware GAN model.

E. Generalizability of PhLR-MBGAN

In the proposed physics-aware GAN design, so far we have demonstrated that the inclusion of upper envelope in the architecture and in loss function has a positive impact on signatures quality and activity recognition performance. But, does this come in for the expanse of generalization capability of the GAN? In other words, does the inclusion of envelope only push the PhLR-MBGAN to the state of complete memorization of the training instances? To answer this, we ran the following experiment: The participants in our study had various heights ranging from 1.57m to 1.905m. We train the PhLR-MBGAN with the data from the shorter participants with the height ranging from 1.57m to 1.67m. We would like to find out whether the GANs can generate synthetic signatures containing the gait properties, i.e., stride duration, of taller participants (height range 1.72m to 1.905m). The time between the consecutive heel strike of the same foot is the stride duration/time. In the case of normal walking, the stride duration of a tall person is higher than the short person. First, we find the stride duration of all the real samples and separate the samples with a stride time of 1.4 seconds or less. Then, we train the GAN with these detached signatures of shorter stride duration. We will investigate whether GAN can generate signatures with stride time higher than 1.4 sec. To find the stride time, the torso velocity (maximum energy at each time index) is first calculated from the spectrograms, as shown in red color at figure 15 (a). Then, the torso acceleration is calculated, by differentiating the torso velocity (figure 15 (b)). This acceleration is filtered with a first-order Butterworth low pass filter of 2Hz cut-off frequency. Each peaks in this figure

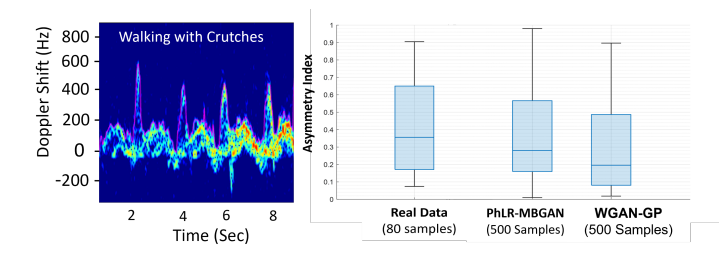


Fig. 14. Comparison of Asymmetry Index of synthetic samples with real samples for the class 'walking with crutches'.

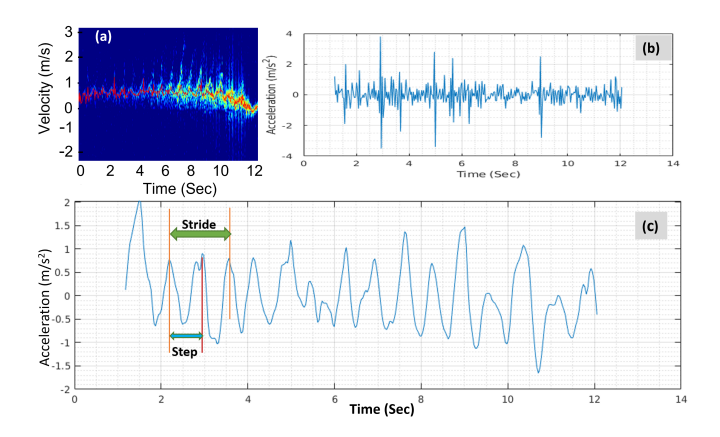


Fig. 15. Finding stride duration. (a) Torso velocity extraction; (b) Torso acceleration; (c) acceleration after butterworth filter

15 (c) is an step [57]. The time gap between two consecutive peaks is step duration and the time gap between every two consecutive even or odd peaks (for example, 1st and 3rd, 2nd and 4th, 3rd and 5th, etc.) are stride duration.

The histograms in Figure 16 depict the real and GAN generated samples distributed over different stride duration. The top right histogram shows the distribution of the training samples with stride rate less than 1.4 sec. The bottom row shows the histograms of GAN generated samples, While training the PhLR-MBGAN and WGAN-GP with these real samples of shorter strides. It is evident from the histograms that the GAN can generate the data with stride duration higher than 1.4 sec. PhLR-MBGAN generates 79 samples with stride duration higher than 1.4 sec out of 500 samples; whereas the WGAN-GP generated 90 samples with stride duration higher than 1.4 sec. The signature that PhLR-MBGAN generates has a maximum stride duration of 1.738 sec, whereas WGAN-GP could generate a maximum stride duration of 1.71 sec. This indicates that even though we are putting more constraint in the loss function and architecture, this does not necessarily restrict the PhLR-MBGAN's generalization capability, nor does it increase the memorization.

VII. CONCLUSION

In this paper, we designed physics-aware GANs to synthesize RF micro-Doppler signatures with enhanced kinematic fidelity. The designed multi-branch GAN (MBGAN) architectures integrate the envelopes of the signatures as the auxiliary branches into the discriminator and add a physicsbased constraint into the discriminator loss function. It was shown that the architectural modification alone can improve the quality of the generated signatures; however, inclusion of both the envelope and physics-based losses provided the most accurate synthetic signatures. The latter were manifested in distinct torso response, accurate Doppler shift and consistent periodicity. We considered classification of 14 different ambulatory activities and showed that training with Single-MBGAN and PhLR-MBGAN, respectively, generated 3% and 6% improvements in comparison with the baseline WGAN-GP. Image quality metrics were applied and affirmed that

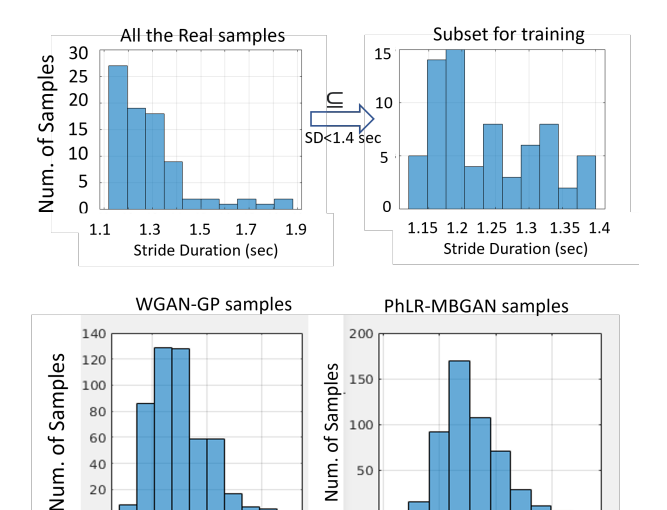


Fig. 16. PhLR-MBGAN generates signatures with stride duration higher than 1.4 sec, even though training samples only contains signatures with stride duration less than 1.4 sec. Adding envelope does not dim off PhLR-MBGAN's ability to generate the variation of training samples.

1.2 1.4 1.6 Stride Duration (Sec)

PhLR-MBGAN generated signatures achieve higher structural similarities and and lower mean square error compared to other variations of MBGAN. Moreover, gait asymmetry present in the real signatures were well replicated in PhLR-MBGAN generated signatures. Finally, our results showed that the modification of architecture and loss function do not constrain the ability of PhLR-MBGAN to generate out-ofsubject variations in the training samples. Although the paper focused on human activities, the proposed synthesis technique can be beneficial to a broad range of applications involving micro-Doppler synthesis, where the maximal instantaneous frequencies underlie the motion's uniqueness.

VIII. ACKNOWLEDGEMENTS

This work was funded in part by National Science Foundation (NSF) Cyber-Physical Systems (CPS) Program Award #1932547. Human studies research was conducted under UA Institutional Review Board (IRB) Protocol #18-06-1271.



20

1.2 1.4 1.6 Stride Duration (Sec)

M. Mahbubur Rahman received the B.S. degree in Electronics and Communication Engineering from Khulna University of Engineering and Technology (KUET), Bangladesh, in 2016. He is currently a Ph.D. candidate in Electrical and Computer Engineering at the University of Alabama (UA), Tuscaloosa, AL, USA, and a research assistant in the UA Laboratory of Computational Intelligence for Radar (CI4R). His research interests include radar signal processing, machine learning, and multimodal sensing for fall detection and gait analysis,

vehicular autonomy and human-computer interaction.

M.M. Rahman is a recipient of the UA Graduate Council Fellowship in September 2020 and 3rd place in the Best Student Paper Competition of the IEEE Radar Conference in April 2021.



Sevgi Z. Gurbuz (S'01-M'10-SM'17) received the B.S. degree in electrical engineering with minor in mechanical engineering and the M.Eng. degree in electrical engineering and computer science from the Massachusetts Institute of Technology, Cambridge, MA, USA, in 1998 and 2000, respectively, and the Ph.D. degree in electrical and computer engineering from Georgia Institute of Technology, Atlanta, GA, USA, in 2009.

From February 2000 to January 2004, she worked as a Radar Signal Processing Research Engineer

with the U.S. Air Force Research Laboratory, Sensors Directorate, Rome, NY, USA. Formerly an Assistant Professor in the Department of ElectricalElectronics Engineering at TOBB University, Ankara, Turkey and Senior Research Scientist with the TUBITAK Space Technologies Research Institute, Ankara, Turkey, she is currently an Assistant Professor in the University of Alabama at Tuscaloosa, Department of Electrical and Computer Engineering. Her current research interests include RF sensor-enabled cyber-physical systems, radar signal processing, physics-aware machine learning, sensor networks, human motion recognition for biomedical, automotive autonomy, and human-computer interaction (HCI) applications. She has recently received a patent in April 2022 relating to radar-based American Sign Language (ASL) recognition.

Dr. Gurbuz is a recipient of the 2022 American Association of University Women Research Publication Grant in Medicine and Biology, the IEEE Harry Rowe Mimno Award for the Best IEEE AES Magazine Paper of 2019, the 2020 SPIE Rising Researcher Award, an EU Marie Curie Research Fellowship, and the 2010 IEEE Radar Conference Best Student Paper Award. Dr. Gurbuz also serves as a member of the IEEE Radar Systems Panel and is an Associate Editor for the IEEE Transactions of Aerospace and Electronic Systems, the newly launched IEEE Transactions on Radar Systems, and the IET Radar, Sonar, and Navigation.



Moeness Amin received the Ph.D. degree from the University of Colorado, Boulder, in 1984. Since 1985, he has been with the Faculty of the Department of Electrical and Computer Engineering, Villanova University, Villanova, PA, USA, where he became the Director of the Center for Advanced Communications, College of Engineering, in 2002.

Dr. Amin is a Life Fellow of the Institute of Electrical and Electronics Engineers (IEEE); Fellow of the International Society of Optical Engineering (SPIE); Fellow of the Institute of Engineering and

Technology (IET); and a Fellow of the European Association for Signal Processing (EURASIP). He is the Recipient of: the 2022-IEEE Dennis Picard Gold Medal in Radar Technologies and Applications; the 2017-Fulbright Distinguished Chair in Advanced Science and Technology; the 2016-Alexander von Humboldt Research Award; the 2016-IET Achievement Medal; the 2014-IEEE Signal Processing Society Technical Achievement Award; the 2009-Technical Achievement Award from the European Association for Signal Processing; the 2015-IEEE Aerospace and Electronic Systems Society Warren D White Award for Excellence in Radar Engineering. He is also the Recipient of the 2010-Chief of Naval Research Challenge Award; the 1997-IEEE Philadelphia Section Award; the 1997-Villanova University Outstanding Faculty Research Award. He is the Recipient of the IEEE Third Millennium

Dr. Amin served as Chair/Member of the Electrical Cluster of Franklin Institute Committee on Science and the Arts (2001-2016). He currently serves on the Editorial Board of the Proceedings of the IEEE. He is the Editor of three books on radar.

REFERENCES

- S. Z. Gurbuz and M. G. Amin, "Radar-based human-motion recognition with deep learning: Promising applications for indoor monitoring," *IEEE Signal Processing Magazine*, vol. 36, no. 4, pp. 16–28, 2019.
- [2] P. Nallabolu, L. Zhang, H. Hong, and C. Li, "Human presence sensing and gesture recognition for smart home applications with moving and stationary clutter suppression using a 60-ghz digital beamforming fmcw radar," *IEEE Access*, vol. 9, pp. 72 857–72 866, 2021.
- [3] S. Abdulatif, Q. Wei, F. Aziz, B. Kleiner, and U. Schneider, "Microdoppler based human-robot classification using ensemble and deep learning approaches," *CoRR*, vol. abs/1711.09177, 2017.
- [4] H. Liang, X. Wang, M. S. Greco, and F. Gini, "Enhanced hand gesture recognition using continuous wave interferometric radar," in 2020 IEEE International Radar Conference (RADAR), 2020.
- [5] S. Z. Gurbuz, A. C. Gurbuz, E. A. Malaia, D. J. Griffin, C. S. Crawford, M. M. Rahman, E. Kurtoglu, R. Aksu, T. Macks, and R. Mdrafi, "American sign language recognition using rf sensing," *IEEE Sensors Journal*, vol. 21, no. 3, 2021.
- [6] V. Chen, The Micro-Doppler Effect in Radar, 2nd Ed. Boston: Artech House, 2019.
- [7] M. Amin, Radar for Indoor Monitoring Detection, Classification, and Assessment. Boca Raton, FL: CRC Press, 2017.
- [8] S. Z. Gurbuz, Deep Neural Network Design for Radar Applications. IET, 2020.
- [9] E. Blasch, U. Majumder, and M. Minardi, "Radar Signals Dismount Tracking for Urban Operations," in *Signal Processing, Sensor Fusion,* and *Target Recognition XV*, I. Kadar, Ed., vol. 6235, International Society for Optics and Photonics. SPIE, 2006, pp. 33 – 41. [Online]. Available: https://doi.org/10.1117/12.666455
- [10] U. Majumder, M. Minardi, E. Blasch, L. Gorham, K. Naidu, T. Lewis, and R. Williams, "Radar signals dismount data production," in *Algorithms for Synthetic Aperture Radar Imagery XIII*, E. G. Zelnio and F. D. Garber, Eds., vol. 6237, International Society for Optics and Photonics. SPIE, 2006, pp. 21 24. [Online]. Available: https://doi.org/10.1117/12.666163
- [11] S. Sundar Ram and H. Ling, "Simulation of human microdopplers using computer animation data," in 2008 IEEE Radar Conference, 2008, pp. 1–6.
- [12] S. S. Ram and H. Ling, "Microdoppler signature simulation of computer animated human and animal motions," in 2008 IEEE Antennas and Propagation Society International Symposium, 2008, pp. 1–4.
- [13] C. Karabacak, S. Z. Gurbuz, A. C. Gurbuz, M. B. Guldogan, G. Hendeby, and F. Gustafsson, "Knowledge exploitation for human microdoppler classification," *IEEE Geoscience and Remote Sensing Letters*, vol. 12, no. 10, pp. 2125–2129, 2015.
- [14] B. Erol and S. Z. Gurbuz, "A kinect-based human micro-doppler simulator," *IEEE Aerospace and Electronic Systems Magazine*, vol. 30, no. 5, 2015.
- [15] P. Khomchuk, I. Stainvas, and I. Bilik, "Pedestrian motion direction estimation using simulated automotive mimo radar," *IEEE Transactions* on Aerospace and Electronic Systems, vol. 52, no. 3, 2016.
- [16] M. S. Seyfioglu, B. Erol, S. Z. Gurbuz, and M. G. Amin, "DNN transfer learning from diversified micro-doppler for motion classification," *IEEE Trans on AES*, vol. 55, no. 5, pp. 2164–2180, 2019.
- [17] S. Vishwakarma, C. Tang, W. Li, K. Woodbridge, R. Adve, and K. Chetty, "Gan based noise generation to aid activity recognition when augmenting measured wifi radar data with simulations," in 2021 IEEE International Conference on Communications Workshops (ICC Workshops), 2021.
- [18] K. Y. Alnujaim I, "Augmentation of doppler radar data using generative adversarial network for human motion analysis," *Healthc Inform Res*, vol. 25(4), 2019.
- [19] H. G. Doherty, L. Cifola, R. I. A. Harmanny, and F. Fioranelli, "Unsupervised learning using generative adversarial networks on micro-doppler spectrograms," in 2019 16th European Radar Conference (EuRAD), 2019, pp. 197–200.
- [20] B. Erol, S. Z. Gurbuz, and M. G. Amin, "Motion classification using kinematically sifted acgan-synthesized radar micro-doppler signatures," *IEEE Trans on AES*, vol. 56, no. 4, pp. 3197–3213, 2020.
- [21] B. Erol, S. Z. Gurbuz, and M. G. Amin, "Gan-based synthetic radar micro-doppler augmentations for improved human activity recognition," in 2019 IEEE Radar Conference (RadarConf), 2019, pp. 1–5.
- [22] M. M. Rahman, E. Malaia, A. C. Gurbuz, D. J. Griffin, C. Crawford, and S. Gurbuz, "Effect of kinematics and fluency in adversarial synthetic data generation for asl recognition with rf sensors," *IEEE Transactions on Aerospace and Electronic Systems*, 2022.

- [23] K. I. L. L. e. a. Karniadakis, G.E., "Physics-informed machine learning," in *Nat Rev Phys.*, vol. 3, 2021.
- [24] R. T. Q. Chen, Y. Rubanova, J. Bettencourt, and D. Duvenaud, "Neural ordinary differential equations," in *Proceedings of the 32nd International Conference on Neural Information Processing Systems*, ser. NIPS'18. Red Hook, NY, USA: Curran Associates Inc., 2018, p. 6572–6583.
- M. Raissi, P. Perdikaris, and G. Karniadakis, "Physicsinformed neural networks: A deep learning framework for solving forward and inverse problems involving nonlinear equations," partial differential Journal Computational of Physics, vol. 378, pp. 686–707, 2019. [Online]. Available: https://www.sciencedirect.com/science/article/pii/S0021999118307125
- [26] Z. Chen, Y. Liu, and H. Sun, "Deep learning of physical laws from scarce data," ArXiv, vol. abs/2005.03448, 2020.
- [27] L. de Oliveira, M. Paganini, and B. Nachman, "Learning particle physics by example: Location-aware generative adversarial networks for physics synthesis," *Computing and Software for Big Science*, vol. 1, no. 1, sep 2017.
- [28] Y. Yang and P. Perdikaris, "Adversarial uncertainty quantification in physics-informed neural networks," *Journal of Computational Physics*, vol. 394, pp. 136–152, oct 2019.
- [29] Z. Yang, J. Wu, and H. Xiao, "Enforcing imprecise constraints on generative adversarial networks for emulating physical systems," Communications in Computational Physics, 2021.
- [30] J. Wu, K. Kashinath, A. Albert, D. B. Chirila, Prabhat, and H. Xiao, "Enforcing statistical constraints in generative adversarial networks for modeling chaotic dynamical systems," *J. Comput. Phys.*, vol. 406, p. 109209, 2020.
- [31] B. Erol, S. Z. Gurbuz, and M. G. Amin, "Synthesis of micro-doppler signatures for abnormal gait using multi-branch discriminator with embedded kinematics," in *IEEE Radar Conf.*, 2020, pp. 175–179.
- [32] M. M. Rahman, S. Z. Gurbuz, and M. G. Amin, "Physics-aware design of multi-branch gan for human rf micro-doppler signature synthesis," in *IEEE Radar Conf.*, 2021, pp. 1–6.
- [33] M. Arjovsky, S. Chintala, and L. Bottou, "Wasserstein gan," 2017.
- [34] Y. Rubner, C. Tomasi, and L. Guibas, "A metric for distributions with applications to image databases," in *Sixth International Conference on Computer Vision (IEEE Cat. No.98CH36271)*, 1998, pp. 59–66.
- [35] D. M. J. E. S. Endres, "A new metric for probability distributions," in IEEE Trans. Inf. Theory., vol. 49, no. 7, 2003.
- [36] I. J. Goodfellow, J. Pouget-Abadie, M. Mirza, B. Xu, D. Warde-Farley, S. Ozair, A. Courville, and Y. Bengio, "Generative adversarial networks," 2014. [Online]. Available: https://arxiv.org/abs/1406.2661
- [37] I. Gulrajani, F. Ahmed, M. Arjovsky, V. Dumoulin, and A. Courville, "Improved training of wasserstein gans," 2017.
- [38] H. Lee, J. Kim, E. K. Kim, and S. Kim, "Wasserstein generative adversarial networks based data augmentation for radar data analysis," *Applied Sciences*, vol. 10, 2020.
- [39] I. Alnujaim, S. S. Ram, D. Oh, and Y. Kim, "Synthesis of microdoppler signatures of human activities from different aspect angles using generative adversarial networks," *IEEE Access*, 2021.
- [40] L. Qu, Y. Wang, T. Yang, and Y. Sun, "Human activity recognition based on wrgan-gp-synthesized micro-doppler spectrograms," *IEEE Sensors Journal*, vol. 22, no. 9, pp. 8960–8973, 2022.
- [41] X. Li, Y. He, and X. Jing, "A survey of deep learning-based human activity recognition in radar," *Remote Sensing*, vol. 11, no. 9, p. 1068, 2019.
- [42] X. Yao, X. Shi, Y. Li, L. Wang, H. Wang, S. Ren, and F. Zhou, "Gmt-wgan: An adversarial sample expansion method for ground moving targets classification," *Remote Sensing*, vol. 14, no. 1, 2022.
- [43] C. Tang, W. Li, S. Vishwakarma, K. Woodbridge, S. Julier, and K. Chetty, "Learning from natural noise to denoise micro-doppler spectrogram," 2021.
- [44] Z. Cui, M. Zhang, Z. Cao, and C. Cao, "Image data augmentation for SAR sensor via generative adversarial nets," *IEEE Access*, vol. 7, 2019.
- [45] S. Z. Gürbüz, "Operational assessment and adaptive selection of micro-doppler features," *IET Radar, Sonar Navigation*, vol. 9, pp. 1196–1204(8), December 2015. [Online]. Available: https://digital-library.theiet.org/content/journals/10.1049/iet-rsn.2015.0144
- [46] A. K. Seifert, M. G. Amin, and A. M. Zoubir, "Toward unobtrusive in-home gait analysis based on radar micro-doppler signatures," *IEEE Transactions on Biomedical Engineering*, vol. 66, no. 9, pp. 2629–2640, 2019.
- [47] B. Erol, M. G. Amin, and B. Boashash, "Range-doppler radar sensor fusion for fall detection," in 2017 IEEE Radar Conference (RadarConf), 2017.

- [48] K. Buchin, M. Buchin, and C. Wenk, "Computing the fréchet distance between simple polygons in polynomial time," in *Proceedings of the* twenty-second annual symposium on Computational geometry, 2006, pp. 80–87.
- [49] Mathworks, "Wiener adaptive filter for noise removal." [Online]. Available: https://www.mathworks.com/help/images/noise-removal.htmlbuh9ylp-72'
- [50] H. Sun, L. Gu, and B. Sun, "Adathm: Adaptive gradient method based on estimates of third-order moments," in 2019 IEEE Fourth International Conference on Data Science in Cyberspace (DSC), 2019, pp. 361–366.
- [51] K.AMANO, "Kaggle: Wgan-gp in keras," 2019. [Online]. Available: 'https://www.kaggle.com/amanooo/wgan-gp-keras/notebook'
- [52] N. Kodali, J. Abernethy, J. Hays, and Z. Kira, "On convergence and stability of gans," *arXiv preprint arXiv:1705.07215*, 2017.
- [53] H. Mitchel, "Image similarity measures," *Image Fusion: Theories, Techniques and Application.*
- [54] Z. W. et.all., "Image quality assessment: from error visibility to structural similarity," *IEEE Trans. Image Processing*, vol. 47, 2004.
- [55] S. Gurbuz, M. Rahman, E. Kurtoglu, T. Macks, and F. Fioranelli, "Cross-frequency training with adversarial learning for radar micro-doppler signature classification," *Proceedings of SPIE*, vol. 11408, pp. 1–11, 2020.
- [56] M. K. Laroche DP, Cook SB, "Strength asymmetry increases gait asymmetry and variability in older women." vol. 44(11), 2012.
- [57] F. Bugané, M. Benedetti, G. Casadio, S. Attala, F. Biagi, M. Manca, and A. Leardini, "Estimation of spatial-temporal gait parameters in level walking based on a single accelerometer: Validation on normal subjects by standard gait analysis," *Computer Methods and Programs in Biomedicine*, vol. 108, no. 1, pp. 129–137, 2012.